MICROVASCULAR HEAT TRANSFER ANALYSIS IN CARBON FIBER COMPOSITE MATERIALS

Thesis

Submitted to

The School of Engineering of the

UNIVERSITY OF DAYTON

In Partial Fulfillment of the Requirements for

The Degree of

Master of Science in Chemical Engineering

By

Matthew Ryan Pierce

Dayton, Ohio

August 2010

UNIVERSITY of DAYTON

MICROVASCULAR HEAT TRANSFER ANALYSIS IN CARBON FIBER COMPOSITE MATERIALS

APPROVED BY:

____
Kevin J. Myers, D.Sc.
Committee Chair
Professor, Chemical and Materials Engineering Department

____
David M. Phillips, Ph.D.
Research Advisor
Universal Technology Corporation, Engineering Division

____
C. William Lee, Ph.D.
Committee Member
Professor, Chemical and Materials Engineering Department

____
Malcolm W. Daniels, Ph.D.
Associate Dean
School of Engineering

____
Tony E. Saliba, Ph.D.
Dean
School of Engineering

ABSTRACT

MICROVASCULAR HEAT TRANSFER ANALYSIS IN CARBON FIBER COMPOSITE MATERIALS

Name: Pierce, Matthew Ryan
University of Dayton

Research Advisor: Dr. David Phillips

Inclusion of a microvascular network of stainless steel tubes into a quasi-isotropic composite laminate constructed of IM7/977-2 prepreg processed under standard autoclave techniques has been accomplished. In addition, a technique was developed to create unlined microvascular channels under the same processing conditions. The focus of this study was to examine the heat transfer properties when a heat transfer fluid flowed through the network. Mode I mechanical testing showed no mechanical penalty for adding microvascular channels to the material. A multiple tube network yielded cooling capabilities up to 3 kW/m^2. A two-dimensional, analytic fit and boundary condition modification were used to determine the bottlenecks for the heat transfer in the hybrid system. It was determined that three-fourths of the total resistance to heat transfer is due to the effects of surface heat transfer and conduction through the panel. There was negligible difference in the heat transfer behavior of the channels created by stainless steel tubes compared to unlined passages.

ACKNOWLEDGEMENTS

Funding for this project was provided by the Air Force Office of Scientific Research (Dr. Byung Lip "Les" Lee, Grant number 09RX02COR). The work was conducted at the Air Force Research Laboratory, Materials and Manufacturing Directorate, Nonmetallic Materials Division, Composite and Hybrid Materials Branch (AFRL/RXBC) through the Southwestern Ohio Council for Higher Education. Dr. David Phillips, a visiting scientist at AFRL/RXBC, working for Universal Technology Corporation Inc., was very involved in all phases of the research. Dr. Jeff Baur and Dr. Dean Foster, both of AFRL/RXBC, provided additional support. Mr. Ron Trejo, University of Dayton Research Institute, contributed valuable technical expertise in sample processing and testing at AFRL. Dr. Kevin Myers and Dr. William Lee, University of Dayton, provided guidance on academic matters. Tuition support was provided by the Dayton Area Graduate Studies Institute.

TABLE OF CONTENTS

LIST OF FIGURES

LIST OF TABLES

LIST OF SYMBOLS

A	Channel cross-sectional area
B	Panel thickness
C_p	Fluid heat capacity
D_1	Inside tube diameter
H	Enthalpy
h	Panel surface heat transfer coefficient
h_1	Fluid to channel interface heat transfer coefficient
k	Panel thermal conductivity
k_t	Tube thermal conductivity
L	Panel length
$\dot{m}$	Fluid mass flow rate
n	Series integer
q	Heat flux
Q	Total heat duty
Q_i	Heat duty inside panel
Q_{panel}	Heat duty from surface of panel
Q_s	Heat duty through surface of panel
$Q_{transfer}$	Heat duty from tube energy balance
Q_{tube}	Heat duty through tube
r_1	Inside tube radius
R_1	Tube interface thermal resistance
$R_{1,2}$	Tube wall thermal resistance
R_2	Tube-composite interface thermal resistance
r_2	Outside tube radius
Re	Reynolds' number
R_i	Internal thermal resistance of panel
R_s	Surface thermal resistance of panel
R_{total}	Total thermal resistance of panel
S_A	Heat transfer surface are of channel

T_0	Ambient temperature
T_{1f}	Inlet fluid temperature
T_{1s}	Surface temperature at inlet
T_{2f}	Outlet fluid temperature
T_{2s}	Panel surface temperature at outlet
T_f	Fluid temperature
T_s	Panel surface temperature
T_{wall}	Surface temperature as "wall" of fin
U	Overall heat transfer coefficient
U_i	Internal heat transfer coefficient
U_s	Surface heat transfer coefficient
u_2	Tube-composite individual heat transfer coefficient
V_y	Volumetric flow rate
W	Panel width
x	Dimensional coordinate
y	Dimensional coordinate
Y	Integration function in terms of y
z	Dimensional coordinate
Z	Integration function in terms of z
β	Constant describing fluid temperature profile
$-\Delta P$	Pressure drop
Θ_f	Dimensionless fluid temperature
Θ_s	Dimensionless surface temperature
λ	Integration constant
μ	Fluid viscosity
ρ	Fluid density

Chapter I: Introduction

Adding additional functionality to traditional composite materials has been a recent goal of the aerospace industry and, in particular, the United States Air Force. Increasing functionality while minimizing additional size and weight can lead to both cost savings and increased mission capabilities. One potential method to achieve this end is to introduce vascular networks into current composite materials used in the aerospace industry. In animals, these small, yet extensive vascular pathways provide a number of advantages including sensing, healing and thermal management. By introducing microvascular pathways, channels with micron-scale diameters, to current aerospace materials, these same advantages can potentially be achieved. It is necessary to explore the current achievements in this area to identify where new research and improvements can be made.

1.1. Microvascular for Sensing

Kousarakis et al. have explored the use of microvascular channels as a sensing tool. They employed a technique called "Comparative Vacuum Monitoring" (CVM). The system is used to monitor damage in laminate composites. The long, narrow channels are situated parallel to one another between the plies of the composite. Every other tube is subject to vacuum, while the rest remain at ambient pressure. A system monitors the pressure in the channels. The channels are placed in such a manner so that, when a crack occurs, it connects the two networks of channels, allowing air to flow between the two. The result, which is detected by the system, is a rise in pressure in the evacuated channel, indicating damage has occurred. [1,2]

The basis of the Kousarakis et al. research was determining the mechanical property impact of creating these channels in the composite. Using a carbon fiber and epoxy prepreg, channels were created by two methods. The first was created by inserting a non-removable glass tube, ranging in diameter from 170-680 µm. The second was created by inserting a silicone mandrels and removing them after curing. These mandrels ranged in diameter from 400-1800 µm. [1,2]

The insertion of the channels affected some of the structural properties of the composite. Mode I delamination toughness actually increased due to a crack blunting effect. The interlaminar shear strength (ILSS), however, decreased. This decrease was found to be linear with the increasing diameter of the channels. The modulus as well as the tensile and compressive strength properties decrease with increasing channel size after a critical size is reached. According to Kousarakis et al., this critical size "lies between ~ 1 and 3 mm for longitudinal and between ~0.3 and 0.7 mm for transverse galleries." Longitudinal refers to the case when the channels are oriented 0º to the applied force, while transverse refers to 90º to the applied force. [1,2]

Pang and Bond explored a different damage detection mechanism. It is sometimes difficult to identify impact induced damage solely by visual inspection. Building on similar work with concrete, their study sought to create a composite that, when damaged, bleeds a "highly conspicuous medium" into the damage site for "enhanced visualization." Their test specimens were glass fiber and epoxy prepreg laminates embedded with 60 µm borosilicate glass tubing. The tubes were filled with UV fluorescent dye and either uncured epoxy resin or hardener (for self-healing tests). Figure 1.1 shows the results of a specimen "after impact damage via indentation and flexural testing." Figure 1-1a shows a standard image of the damage. Figure 1-1b shows an image of the specimen irradiated with UV light. It is clear that UV dye has bled into the internal damage sites highlighting damage which is normally undetected by visual inspection. [3,4]

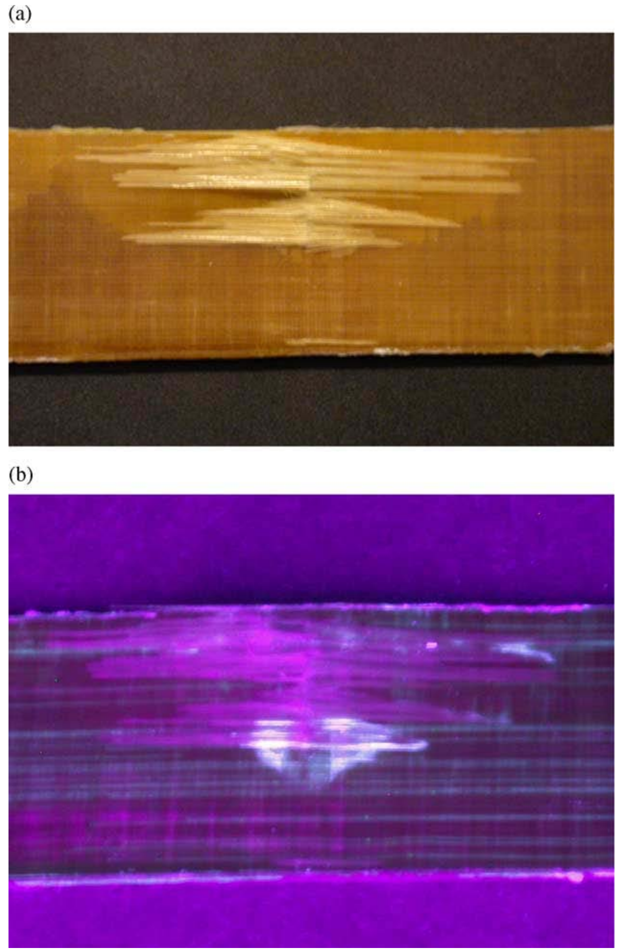

Figure 1-1: Comparison of traditional damage image(a) to ultraviolet illuminated damage(b).[3]

1.2. Microvascular for Healing

Dry performed some of the early microvascular healing work on polymer composites. Glass pipette tubes, four inches long and 100-µl in volume, were embedded, in pairs, in small epoxy resin samples. One was filled with resin and the other was filled with hardener in each pair of tubes. After impact testing, the broken tubes were allowed to leak their contents into the cracks. Upon retesting 8 months later, it was shown that strength was regained, indicating crack repair. [5]

Motuku et al. performed similar experimentation to Dry. Motuku also used glass micro-pipets to deliver healing fluid. The tubes were embedded in a glass fiber and epoxy laminate. The study found that the presence of the "storage tubes did not alter the impact response of the composites." It also showed that repair solution was successfully distributed. [6]

Bleay et al. attempted to create an entire composite with fibers that offered the potential for healing material storage. For the study, composite panels were created using a glass fiber epoxy prepreg. The fibers were hollow 15 μm OD, 5 μm ID. A vacuum pump was used to draw the resin into the hollow fibers, however, only half of the theoretical volume was able to be filled with repair resin. Using a one-part resin repair system seemed to cure rapidly and block the ends of the tubes. The study found that filling the fibers with resin did not alter the impact behavior. Further, it was found that, while some strength was restored, the recovered strength was still much lower than an undamaged panel, indicating minimal healing. [7]

Pang and Bond also investigated self-repair using the same system previously mentioned in their work with UV dye as a means of damage detection. The study was able to show that a "significant fraction of lost mechanical strength is restored by the self-repairing effect". The work further showed that the healing effect decreases over time, which the study attributed to additives in the healing resin. [3,4]

Trask and Bond furthered the work, using a system similar to the work of Pang and Bond. The system consisted of a glass fiber and epoxy prepreg composite with glass tubes containing the healing fluid. However, they added an important processing step: the autoclave. For most aerospace applications, the system must be able to survive an autoclave in order to be considered practical. Pang and Bond were able to autoclave their samples following resin infusion into the glass tubes. This study found that, while there was a 16% reduction in initial strength due to the addition of the glass tubes, "after healing of the damage site was undertaken it was found that a self-healed laminate had a residual strength of 87% compared to an undamaged baseline laminate and 100% compared to an undamaged self-healing laminate." [8]

Williams, Trask and Bond furthered this research. Hollow glass fibers were still used to contain the healing resin, but they were embedded this time in a carbon fiber and epoxy resin prepreg. Nearly 89% of the baseline laminate strength was recovered by self-healing. [9]

To this point, the previously mentioned self-healing systems were all pre-loaded with healing resin. Williams, Trask, and Bond explored a sandwich composite system that allowed healing fluid to be inserted after damage has occurred. A polymethacrylimide closed-cell foam was used as the core material. PVC tubing 2.5 mm OD, 1.5 mm ID was iembedded in the middle of the core. Holes, 1.5 mm in diameter, were drilled through the core and into the tubes, creating risers to the face sheets. The face sheets were composed of a glass fiber and epoxy prepreg laminate. Figure 1-2 shows the stepwise manufacturing procedure. The study showed injecting a premixed epoxy resin system into a damaged composite restored nearly all of the undamaged strength. Injecting unmixed resin components into the damaged composite and allowing the components to mix in the damage site was able also able to restore original strength in the cases where both components flowed into the damage site. In about half of the cases, however, only one component penetrated the damaged area,

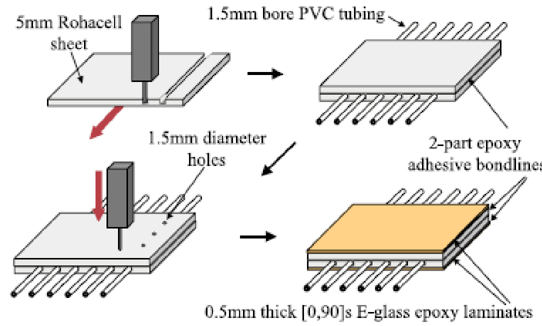

Figure 1-2. Manufacture of vascular sandwich panels [10]

which led to no healing. In later testing, Williams et al. were able to enhance mixing of the unmixed resin and hardener in the damage sites by maintaining a pressure of $3x10^5$ Pa. [10,11]

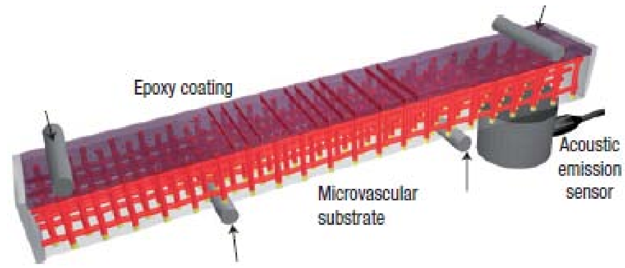

Figure 1-3. 3D microvascular network [12]

Toohey et al. used direct ink writing to form a 3D vascular network. The direct ink writing technique was used to deposit an organic ink in a three-dimensional microvascular scheme. Once deposited, the 3D network is infiltrated with an epoxy resin to serve as the matrix. Once cured, the ink is removed via heating and slight vacuum. This leaves behind a network of microvascular channels, shown in Figure 1-3. The surface of the network is then coated with a Grubbs' catalyst/epoxy resin mixture. Wax was used to fill the microvascular passages so that the catalyst mixture did not flow into the channels. A monomeric fluid of dicyclopentadiene (DCPD) was injected into the channels. Upon fracture, the healing fluid flowed through the cracks and, once it reached the Grubbs' catalyst at the surface, cured to heal the cracking. In addition, the nature of the microvascular network allowed the DCPD to be reloaded following healing. This enabled Toohey et al. to run seven separate healing cycles per sample, each with a healing efficiency between 30-70%. [12]

Toohey et al. built on this technique in later research. Using the same direct ink writing technique, a microvascular network was formed. However, by using a photocurable resin and selectively filling in key sections of the network by photopolymerization, it was possible to isolate sections of the network. This allowed for the use of a two part epoxy resin system. Each part was isolated in its segment of the network until a surface crack occurred. The epoxy resin and hardener would then flow into the crack, mix, and cure, healing the crack. Up to 16 separate healing cycles were possible with healing efficiencies of over 60% in some cases. [13]

Hansen et al. further explored the use of the direct ink writing technique to create microvascular networks. By using two different inks with different melting temperatures, a more precise interpenetrating network was created. Using a two-part epoxy resin and hardener system, 50% healing efficiency was maintained for 30 healing cycles. [14]

1.3. Microvascular for Thermal Management

Tuckerman and Pease investigated the use of fluid flowing through microvascular channels as a means of cooling integrated circuits. They found that this type of heat transfer was limited by the heat transfer coefficient between the cooling fluid and the substrate. The study also determined that, since this heat transfer coefficient is inversely proportional to channel width, decreasing channel size will increase cooling efficiency [15]

Ashman and Kandlikar reviewed some of the common techniques available to create a microchannel heat exchanger. Micromachining allows a wide range of materials to be processed by using tools to cut, grind, bond etc. in order to create microchannels. Diffusion bonding is a form of micromachining that involves welding together two surfaces under high temperature and pressure in a vacuum or inert environment. This technique is used to bond together two sides of a heat exchanger with channels already formed. Stereolithography is a technique used to create more intricate networks. UV light is shown through a photoreactive liquid polymer. This polymer solidifies in a thin layer. Successive layers are created by this process. The solid polymer part is then made into a ceramic by pyrolysis. Chemical etching uses a strong acid or base to create the microchannels by removing the material of a substrate. The substrate removal rate must be highly directional. For example, in silicon wafers, the removal rate is 600 times faster in one direction compared to the perpendicular direction. A process known as LIGA projects X-rays through a screen of desired orientation onto a photo-resist material that is sensitive to X-rays. The photo-resist material is bonded to a conductive material. After exposure, the two materials are placed in a nickel ion solution. Based on the orientation of the screen, the nickel is electroplated onto the photo-resist material. This creates the desired nickel structure that can be used on its own or connected with other structures to create a microchannel heat exchanger. [16]

Paul et al. created a microchannel heat exchanger by laser micromachining channels into successive layers and then using diffusion bonding to join all of the layers [17]. The CO_2 laser ablation method was used by Qi et al. to create channels in a polycarbonate substrate [18]. Lee et al. investigated the heat transfer behavior of rectangular microchannels [19] . The test specimens were made of copper with microchannel widths from 194 μm to 534 μm. Reynolds umbers ranged from 300 to 3500. Lelea et al. performed similar work on 100 μm to 500 μm diameter stainless steel microtubes [20].

Wei et al. further explored the use of microchannel heat exchangers for cooling microelectronics. A multi-layer heat exchanger was created using deep reactive ion etching on silicon wafers. The heat exchanger was capable of running both parallel and countercurrent flow. [21]

Oueslati et al. investigated the use of microchannel heat exchangers in cooling printed circuit boards. The direct write method was used to create the microchannels that are integrated into the structure of the circuit board. [22]

Kozola et al. created a thin fin microvascular sample using bulk polymer. The study explored both single layer and three-dimensional networks. The direct ink writing technique was used to create the networks. An infrared camera was used to capture thermal data while exploring the effects of channel size and flow rate. [23]

1.4. Goals of this Project

Little has been accomplished in the area of incorporating microvascular pathways into typical carbon fiber and epoxy composites used in aerospace applications. Most of the processing of these microvascular networks is accomplished without regard to standard autoclave processing techniques. Further, much of the heat transfer analysis of microvascular networks is associated with microelectronics. The goal of this research will be to develop a microvascular network using typical aerospace composite materials and standard autoclave processing techniques. In addition, the heat transfer properties of this system will be evaluated.

Chapter II: Experimental Set-Up and Data Collection

2.1. General Panel Construction

A typical aerospace carbon fiber and epoxy composite, unidirectional IM7/977-2 prepreg (Cytec Industries Inc.), was used to construct all mechanical and thermal testing samples. The samples were cured in an autoclave. The pre-impregnated carbon fiber and epoxy sheets were cut and layered as desired before being bagged in Teflon for the autoclave. The samples were placed flat on the autoclave table with a caul plate on top of the layup. The autoclave applied a vacuum to the samples at a differential pressure of 0.69 MPa. The temperature was raised to 179°C at a rate of 2.78 °C/min. This temperature was maintained for 6 hours, and then the autoclave was cooled at a rate of 2.78 °C/min to 60°C. At this point, the autoclave was depressurized and then opened to the atmosphere.

2.2. Mechanical Testing Samples

For the Mode I testing samples, the prepreg was cut into 0.305m x 0.305m squares and twenty-four layers were assembled in a unidirectional manner according to ASTM D5528-01. Matte finish, 304 stainless steel wires (Malin Company Inc.) with diameters of 102, 203, and 406μm (0.004, 0.008, and 0.016 in) were used to simulate hollow tubes. The wires were cleaned with acetone, annealed in a nitrogen atmosphere to straighten them, and then spaced every 6.35mm under tension for insertion at the midplane of the test panels. A 0.07mm thick, 32mm wide Teflon strip was placed perpendicular to the fiber tows at the panel midplane edge as a crack initiator. The final layup was $[0]^{12}$[wires]$[0]^{12}$, with the wires placed at 0°, 45°, and 90° to the fiber tows. A control panel was manufactured with the same laminate layup and crack initiator, but no wires. A second control panel, referred to as 203µm (tube), was manufactured with the same laminate layup and 203µm outer diameter and 102µm inner diameter 304 stainless steel tubes (K33R, K-tube Corporation) placed 90° to the fiber tows.

The panels were faced with a gas permeable Teflon release ply on both sides and then a gas impermeable Teflon release ply. A caul plate was placed on top and the entire assembly was wrapped in impermeable Teflon. Slits were made in the sides to accommodate the protruding wires. Resin seepage was not an issue during curing. All cured panels were inspected with x-ray and C-scan for wire alignment and panel integrity.

All of the Mode I panels were trimmed at the edges and cut into testing coupons 25.4mm wide and 152mm long. The tops and bottoms of the sides with the crack initiators were sanded and cleaned before piano hinges were affixed with the hinge axis even with the end of the crack initiator. The sides of the panel were coated with white paint and marked with a distance scale from the end of the crack initiator to monitor crack length during Mode I testing.

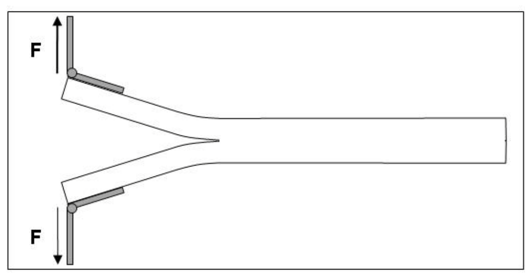

Figure 2-1: Mode I testing

The Mode I samples were mounted on an MTS load frame for testing. The displacement rate was controlled at 1.27mm/min with a force and displacement recorded at 10Hz for both the initial crack opening and the crack propagation. The initial crack was opened to a length as close to 38.1mm as possible. The testing proceeded is shown in Figure 2-1. The data collection for the 0° and no wire samples exhibited smooth crack opening as expected in ASTM D5528-01. The 45° and 90° wire samples did not behave ideally and produced a saw tooth load vs. displacement curve. The crack opening would run and stop in those cases. The crack lengths for the run stops were recorded to interpret the crack opening data.

2.3. Thermal Samples - Multiple Tube Panels

The multi-tube thermal panels were made up of 8 layers of IM7/977-2, 152mmx152mm in size. The quasi-isotropic layup pattern was [90][45][-45][0][tubes][0][-45][45][90]. For these panels, 304 stainless steel tubes were used. Twenty-four (24) 178 mm long tubes with 102 µm OD/ 203 µm OD were placed 6.4 mm apart parallel to one another across the width of the panel, with the first tube 3.2 mm in from the edge. The tubes were placed parallel to the adjacent fiber tows so that the tubes would embed in the adjacent plies. Like the mechanical samples, x-ray and C-scan were performed.

In order to collect the tubes into a single inlet and outlet, flexible PEEK tubing (Valco Instruments Co. Inc., 254 µm ID, 794 µm OD) was attached to the exposed 12.7 mm of stainless steel tubing on either side of the panel. An UV curing adhesive (Loctite 3105, Henkel Corporation, Rocky Hill, CT) was used to attach the PEEK tubing to the stainless steel tube. The PEEK tubing was staggered in length (152mm to 126 mm) to make collecting the tubes less difficult. There was concern that this would lead to unbalanced flow distribution amongst the tubes, but the Hagen-Poiseuille equation showed that this length difference would result in less than 2% difference in flow rate between the longest and shortest tubes.

The 24 tube ends on each side were bundled and held together using a two-part epoxy adhesive (Araldite 2011, Huntsman Advanced Materials, Inc., Los Angeles, CA). The bundled tubes were then inserted into a 25.4 mm 316 stainless steel tube with 6.35 mm OD. The tube bundle was potted in the stainless steel tube with Epon 862/ Jeffamine D-230. Yor-lok fittings were then attached to the stainless steel tube for testing purposes. A picture of the finished panel is shown in Figure 2-2.

Figure 2-2: Multiple tube panel

2.4. Thermal Samples – Single Tube Panels

The layup is the same as for the multiple tube panels. However, instead of 24 tubes across the width of the panel, a single tube was placed in the middle of the panel, parallel to the fiber tows. Panels with both lined and unlined passages were created. The lined panels consisted of three different sizes of 304 stainless steel tube: 102 μm ID/203 μm OD, 127 μm ID/ 254 μm OD, and 254 μm ID/406 μm OD. The tubes extended beyond the edges of the panel (~10-30 mm). This allowed a larger (1.6mm OD) stainless steel tube to be soldered around the smaller tubes, so that 1.6 mm Yor-lok fittings could be attached for plumbing purposes.

To create the panels with unlined passages, 254 μm, 304 stainless steel wire was coated with graphite and then placed in the lay-up. The graphite coating process consisted of spraying the wire with a dry graphite lubricant (Sprayon S00204). Each wire was coated three times. The wires were allowed to dry for approximately ten minutes between each coating. The wire was held under tension during curing. After curing, the wire was extracted and 24 mm long 304 stainless steel tubes with 102 μm ID/203 μm OD were inserted 5 mm into the ends of the passage and affixed with Araldite 2011. Larger (1.6 mm OD) stainless steel tubes were soldered around the smaller tubes so that Yor-lok fittings could be attached.

2.5. Thermal Testing – Multiple Tube Panels

The working fluid in these tests was water. The panels were placed in a convection oven (Memmet UFE 400, Memmert GmbH, Germany) to control the atmospheric temperature and the inlet temperature was controlled by a temperature bath. All exposed sections of tubing were insulated with 25.4 mm fiberglass insulation to ensure that heat transfer only occurred at the panel surface. The mass flow rate through the panels was controlled by an Isco 100DM syringe pump, with a maximum flow rate of 25 ml/minute. At the inlet of the panel, the temperature of the fluid was measured with a type K thermocouple and the pressure was measured with a pressure transducer (Omega PX01C1-500G5T). At the outlet, the temperature was also measured with a type K thermocouple and the fluid was released to atmospheric pressure. These measurements give pressure drop across the panel as well as the total heat load on the panel. The surface temperature profile of the panel was also measured through a sapphire window (Hawk IR, C-type) in the oven using a FLIR model SC620 camera (FLIR Systems, Inc., Wilsonville, OR) with a 620x480 pixel array. The panel gives a two-dimensional temperature profile of the surface of the panel. The emissivity of the panel was determined by holding the panel at five isothermal set points and calibrating to the measured temperature.

2.6. Thermal Testing – Single Tube Panels

Water remained the working fluid for these tests. However, unlike the multiple tube panels, these panels were tested outside of the oven at room temperature. The panels were placed horizontally in order to achieve consistent natural convection conditions across the panel for maximum symmetry and to maintain an equal split of the heat flux in both halves of the panels. The inlet temperature was varied and controlled by a temperature bath. Flow rate was controlled by the same syringe pump. The inlet temperature and pressure, as well as the outlet temperature, were measured by the same means. The infrared camera was also used to measure the two-dimensional surface temperature profile.

For these panels, isothermal pressure drop data was also taken in the convection ovens. The temperature bath and convection oven were used to maintain a uniform inlet and outlet temperature. The infrared camera was still used to ensure that the panel was at an isolated condition.

Chapter III: Data Analysis

3.1. Mechanical Results

Figure 3-1 gives a sample of the data from the Mode I testing based on ASTM D5528-01. The smooth red line shows the load versus displacement of the sample in which the wires are parallel to the adjacent fiber tows. This data matches the control sample data. The jagged blue line shows test data from a sample in which the wire is oriented 90° to the fiber tows. The graph shows that, in the 90° orientation, the wires perform the role of crack blunting, stopping the progress of the crack. The load builds until a certain

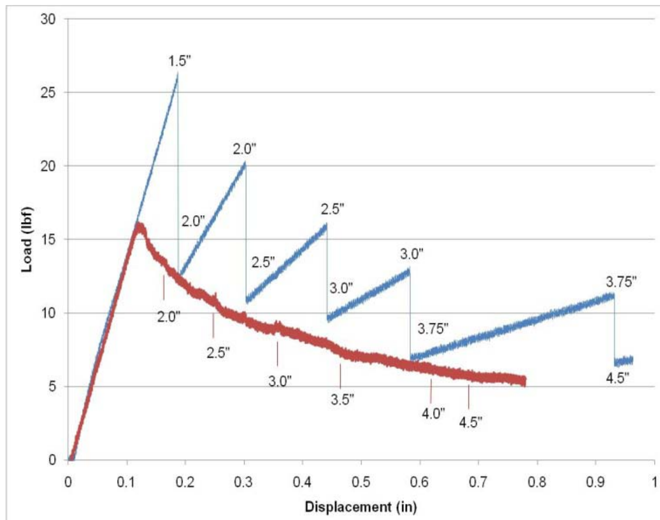

Figure 3-1: Mode I test data comparing the control sample (in red) to a test sample (in blue)

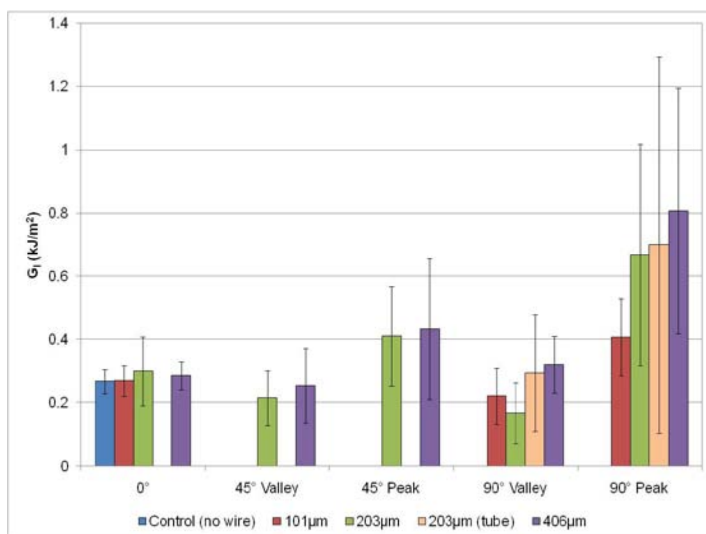

Figure 3-2: Tube side energy balance

point is reach and the crack proceeds to another resin pocket. This was also clear while observing the tests. The load would build until a pop was heard, as the crack ran to another resin pocket, sometimes skipping wires in the process. Figure 3-2 shows that the Mode I moduli for the embedded wire and tube samples are comparable to the control group.

3.2. Thermal Results - Multiple Tube Panels

Thermal images from the multiple tube panel are shown in Figure 3-3. The oven was held at 110 ºC and the inlet temperature was 40 ºC for the flow rate progression pictured. At a flow rate of 24 mL/min, which is an average of 1 mL/min per tube, the surface temperature was cooled by as much as 50 ºC. Figure 3-4 shows the average heat duty as a function of flow rate

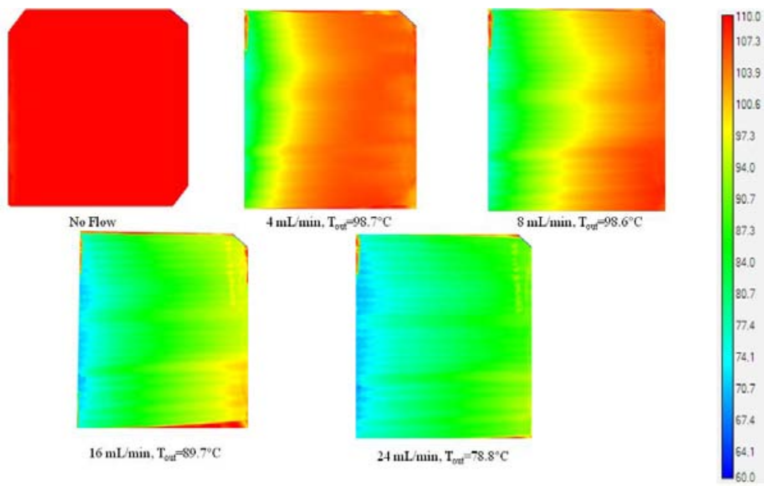

Figure 3-3: Thermal images for various flow rates. Inlet temperature is 40 ºC and oven temperature is 110 ºC.

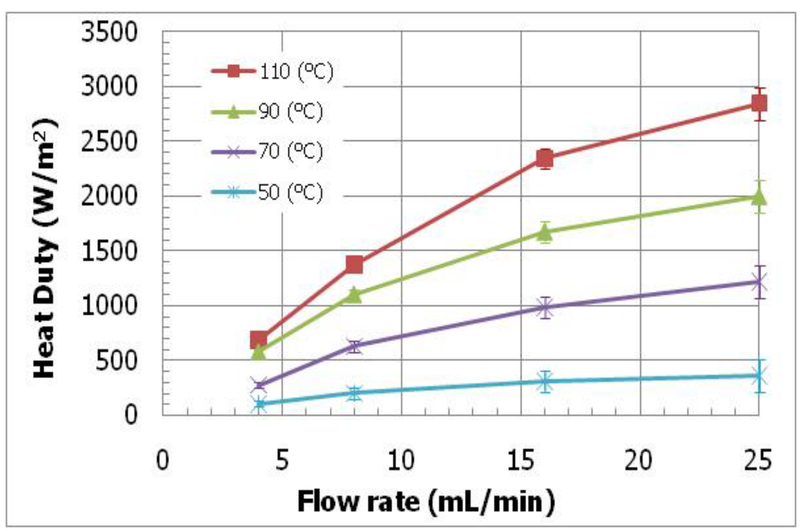

Figure 3-4: Heat duty as a function of flow rate and oven temperature for the multiple tube panel. Inlet temperature is 40 ºC

and oven temperature. The inlet temperature was held at 40 ºC. A heat duty of almost 3 kW/m^2 was achieved at 24 mL/min and an oven temperature of 110 ºC.

3.3. Thermal Results – Single Tube Panels

3.3.1. Single Tube Temperature Profile

Initially, a differential energy balance was performed on the water in the tube. Plug flow in the tube was assumed. The overall heat transfer coefficient, *U*, was assumed to be constant for the entire length of the tube. Figure 3-5 shows the energy balance, also shown in Equation 3-1, where *H* is the enthalpy of the fluid, $Q_{transfer}$ is heat flow due to heat transfer, and $\dot{m}$ is the mass flow rate of the fluid. This balance assumes steady state.

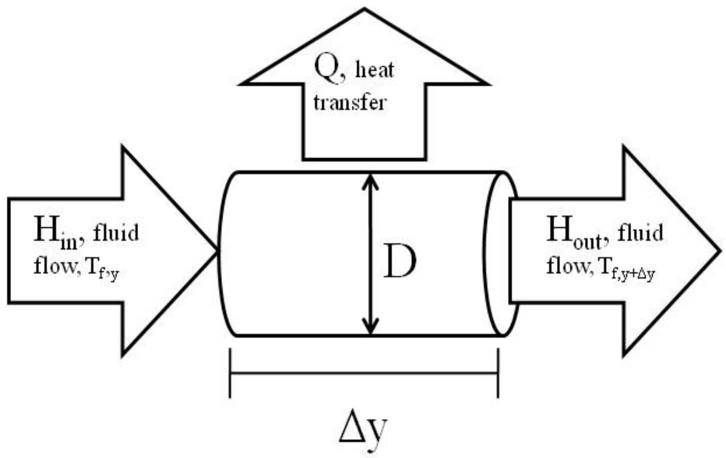

Figure 3-5: Fluid energy balance

$$\dot{m}H_{in,flow,T_{f,y}} - \dot{m}H_{out,flow,T_{f,y+\Delta y}} - Q_{transfer} = 0 \qquad (3\text{-}1)$$

The energy change between the *y* and *y*+Δ*y* is equal to the change in enthalpy between the inlet and outlet, assuming constant fluid velocity and negligible gravitational potential. The change in enthalpy can be expressed by the temperature difference multiplied by the heat capacity (C_p) and the mass flow rate, $\dot{m}$. Mass flow rate is equal to $\rho V_y A$, where ρ is fluid density, V_y is volumetric flow rate, and *A* is tube cross-sectional area. $Q_{transfer}$ is expressed as a function of the temperature difference between the fluid (T_f) and the atmosphere (T_0) with overall heat transfer coefficient, *U*, and heat transfer surface area, S_A. These substitutions lead to Equation 3-2. The heat transfer coefficient and atmospheric temperature are held constant.

$$(\rho C_p V_y A)(T_{f,y} - T_{f,y+\Delta y}) - US_A(T_f - T_0) = 0 \tag{3-2}$$

Dividing by Δy and taking the limit as Δy goes to zero yields the differential equation shown in Equation 3-3, where D_1 is the inside diameter of the tube and $S_A = \pi D_1 \Delta y$.

$$\left(\frac{\rho C_p V_y \pi D_1^2}{4}\right)\frac{dT_f}{dy} + U\pi D_1(T_f - T_0) = 0 \tag{3-3}$$

Simplification leads to

$$\frac{dT_f}{dy} + \frac{4U}{\rho C_p V_y D_1}(T_f - T_0) = 0 \tag{3-4}$$

The group of constant coefficients is combined into a single constant, β. Equation 3-5 is a first order, linear differential equation.

$$\frac{dT_f}{dy} + \beta T_f - \beta T_0 = 0 \tag{3-5}$$

Multiplying by the integration factor, $e^{\beta y}$, leads to Equation 3-6.

$$\frac{dT_f}{dy}e^{\beta y} + \beta T_f e^{\beta y} - \beta T_0 e^{\beta y} = 0 \tag{3-6}$$

Equation 3-6 simplifies to

$$\frac{dT_f e^{\beta y}}{dy} = \beta T_0 e^{\beta y} \tag{3-7}$$

Integration of Equation 3-7 leads to Equation 3-8.

$$T_f e^{\beta y} = T_0 e^{\beta y} + C \tag{3-8}$$

By applying the boundary condition at $y=0$, $T_f = T_{1f}$, where T_{1f} is the inlet fluid temperature the constant C can be determined.

$$C = T_{1f} - T_0 \tag{3-9}$$

Inserting C into the original expression gives Equation 3-10.

$$T_f = T_0 + \left(T_{1f} - T_0\right)e^{-\beta y} \tag{3-10}$$

Rewriting this in terms of dimensionless temperature, θ_f, yields

$$\theta_f = \frac{T_f - T_0}{T_{1f} - T_0} = e^{-\beta y} \tag{3-11}$$

3.3.2. Two-dimensional Fin Analysis

By using this temperature profile, the panels can now be analyzed as two-dimensional fins operating at steady state. Figure 3-6 shows the variables and coordinate system of the fin.

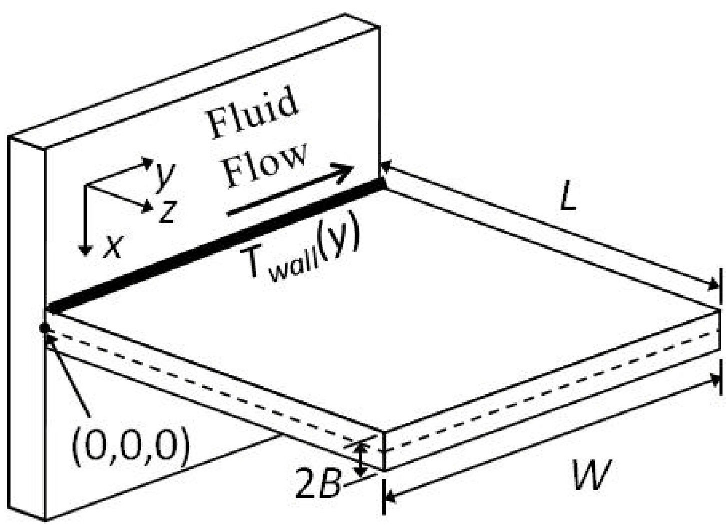

Figure 3-6: Cooling fin geometry

The "wall" of the fin is the middle of the panel directly above the tube, where the maximum temperature deviation from the ambient is present. This temperature profile will serve as the "wall" temperature in the analysis. Each panel has two fins, one on either side of the tube. The fins are identical due to symmetry. This model assumes a constant surface heat transfer coefficient, *h*, as well as constant temperature in the *x*-direction because the thickness of the panel is much less than the length and width.

An energy balance on a panel, as shown in Figure 3-7, gives Equation 3-12, where *q* is heat flux.

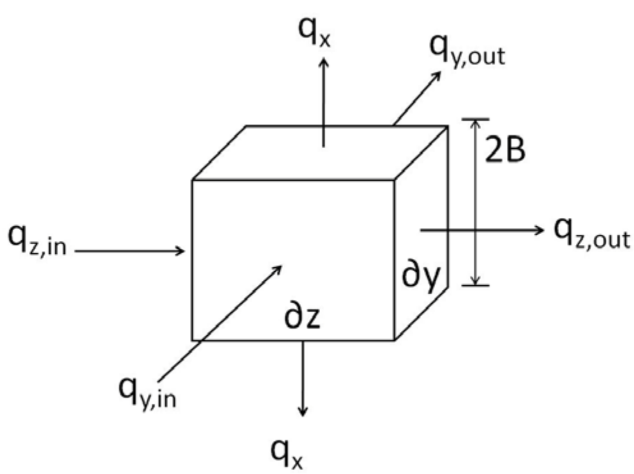

Figure 3-7: Cooling fin energy balance

$$2B\partial q_y \partial z + 2B\partial q_z \partial y + 2q_x \partial y \partial z = 0 \quad (3\text{-}12)$$

Inserting Newton's law of cooling, assuming a constant surface heat transfer coefficient across the panel yields

$$-2B\partial q_y \partial z - 2B\partial q_z \partial y = 2h(T_s - T_0)\partial y \partial z \quad (3\text{-}13)$$

where T_s is surface temperature. Simplification leads to Equation 3-14.

$$-\frac{\partial q_y}{\partial y} - \frac{\partial q_z}{\partial z} = \frac{h}{B}\left(T_s - T_0\right) \tag{3-14}$$

By using Fourier's law of heat conduction, Equation 3-15, the expression in Equation 3-18 is developed, neglecting conduction in the *x*-direction, where *k* is the panel thermal conductivity, which is assumed constant.

$$\overline{q} = -k\nabla T_s \tag{3-15}$$

$$\nabla \cdot \overline{q} = -k\nabla^2 T_s \tag{3-16}$$

$$\frac{\partial q_x}{\partial x} + \frac{\partial q_y}{\partial y} + \frac{\partial q_z}{\partial z} = -k\left(\frac{\partial^2 T_s}{\partial x^2} + \frac{\partial^2 T_s}{\partial y^2} + \frac{\partial^2 T_s}{\partial z^2}\right) \tag{3-17}$$

$$-\frac{\partial q_y}{\partial y} - \frac{\partial q_z}{\partial z} = k\left(\frac{\partial^2 T_s}{\partial y^2} + \frac{\partial^2 T_s}{\partial z^2}\right) \tag{3-18}$$

Inserting Equation 3-18 back into Equation 3-14 leads to

$$k\left(\frac{\partial^2 T_s}{\partial y^2} + \frac{\partial^2 T_s}{\partial z^2}\right) = \frac{h}{B}\left(T_s - T_0\right). \tag{3-19}$$

Rearranging Equation 3-19 gives

$$\frac{\partial^2 T_s}{\partial y^2} + \frac{\partial^2 T_s}{\partial z^2} = \frac{h}{Bk}\left(T_s - T_0\right). \tag{3-20}$$

The three boundary conditions below assume that there is negligible heat transfer from the three edges of the cooling fin.

$$\frac{\partial T_s}{\partial y} = 0\Big|_{y=0}, \quad \frac{\partial T_s}{\partial y} = 0\Big|_{y=W}, \quad \frac{\partial T_s}{\partial z} = 0\Big|_{z=L} \tag{3-21 - 3-23}$$

The final boundary condition states that the temperature profile at z=0, or T_{wall}, is some function of y. T_{1s} is the surface temperature above the fluid inlet, while T_{2s} is the surface temperature at the outlet.

$$T_s(y,z)\big|_{z=0} = f(y), \quad \text{where } f(0) = T_{1s}, \quad f(W) = T_{2s} \tag{3-24}$$

A dimensionless surface temperature, θ_s, will be substituted for T, as shown below, resulting in Equation 3-28.

$$\theta_s = \frac{T_s - T_0}{T_{1s} - T_0} \tag{3-25}$$

$$\partial\theta_s = \frac{\partial T_s}{T_{1s} - T_0} \tag{3-26}$$

$$\partial^2\theta = \frac{\partial^2 T_s}{T_{1s} - T_0} \tag{3-27}$$

$$\frac{\partial^2\theta_s}{\partial y^2} + \frac{\partial^2\theta_s}{\partial z^2} = \frac{h}{Bk}\theta_s \tag{3-28}$$

The separation of variables technique is employed in which the dimensionless temperature, θ, is rewritten as the product of two separable functions of y and z.

$$\theta_s(y,z) = Y(y)Z(z) \tag{3-29}$$

This leads to Equation 3-30.

$$Y''Z + YZ'' = \frac{h}{Bk}YZ \tag{3-30}$$

Simplification yields

$$\frac{Y''}{Y} = \frac{h}{Bk} - \frac{Z''}{Z} \,.. \tag{3-31}$$

The left side of the equation is only a function of *y* and the right side is solely a function of *z*. Holding *z* constant, the left side remains constant as *y* changes. In addition, if *y* is held constant, the right side will stay the same as *z* changes. Therefore, both the left and right hand sides of the equation must be equal to the same constant, denoted by $-\lambda$. This leads to Equation 3-32.

$$\frac{Y''}{Y} = \frac{h}{Bk} - \frac{Z''}{Z} = -\lambda \tag{3-32}$$

This can be broken down into two equations in terms of *y* and *z*, respectively.

$$Y'' + \lambda Y = 0 \tag{3-33}$$

$$Z'' - \left(\lambda + \frac{h}{Bk}\right) Z = 0 \tag{3-34}$$

Rewriting the two *y*-dependent boundary conditions leads to.

$$Y'(0) = Y'(W) = 0 \tag{3-35}$$

In order for Equation 3-33 to satisfy the boundary conditions from Equations 3-21 and 3-22, λ must be one of the eigenvalues

$$\lambda_n = \left(\frac{n\pi}{W}\right)^2, \text{ n=1, 2, 3,…,}\infty. \tag{3-36}$$

The eigenfunction that corresponds to the these eigenvalues is

$$Y_n(y) = \cos\left(\frac{n\pi y}{W}\right). \tag{3-37}$$

Rewriting Equation 3-34 based on the possible eigenvalues of λ

$$Z_n'' - \left(\left(\frac{n\pi}{W}\right)^2 + \frac{h}{Bk}\right) Z_n = 0 \tag{3-38}$$

Rewriting the third, *z*-dependent boundary condition leads to

$$Z_n'(L) = 0 \quad . \tag{3-39}$$

Solving Equation 3-38 for Z_n gives Equation 3-40, where n=1, 2, 3,…, ∞.

$$Z_n(z) = \frac{A_0}{2} + A_n \cosh\left(\left(\left(\frac{n\pi}{W}\right)^2 + \frac{h}{Bk}\right)^{\frac{1}{2}} z\right) + B_n \sinh\left(\left(\left(\frac{n\pi}{W}\right)^2 + \frac{h}{Bk}\right)^{\frac{1}{2}} z\right) \tag{3-40}$$

Taking the derivative of Equation 3-40 leads to

$$Z_n'(z) = \left(\left(\frac{n\pi}{W}\right)^2 + \frac{h}{Bk}\right)^{\frac{1}{2}} \left[A_n \sinh\left(\left(\left(\frac{n\pi}{W}\right)^2 + \frac{h}{Bk}\right)^{\frac{1}{2}} z\right) + B_n \cosh\left(\left(\left(\frac{n\pi}{W}\right)^2 + \frac{h}{Bk}\right)^{\frac{1}{2}} z\right)\right] \tag{3-41}$$

Rewriting the third, z-dependent boundary condition leads to

$$Z_n'(L) = 0 \quad . \tag{3-42}$$

Applying this boundary condition gives

$$Z_n'(L) = 0 = A_n \sinh\left(\left(\left(\frac{n\pi}{W}\right)^2 + \frac{h}{Bk}\right)^{\frac{1}{2}} L\right) + B_n \cosh\left(\left(\left(\frac{n\pi}{W}\right)^2 + \frac{h}{Bk}\right)^{\frac{1}{2}} L\right) . \tag{3-43}$$

Solving for the constant B_n yields

$$B_n = \frac{-A_n \sinh\left(\left(\left(\frac{n\pi}{W}\right)^2 + \frac{h}{Bk}\right)^{\frac{1}{2}} L\right)}{\cosh\left(\left(\left(\frac{n\pi}{W}\right)^2 + \frac{h}{Bk}\right)^{\frac{1}{2}} L\right)} \quad . \tag{3-44}$$

Substituting B_n back into Equation 3-40 leads to

$$Z_n(z)=\frac{A_0}{2}+A_n\left[\cosh\left(\left(\left(\frac{n\pi}{W}\right)^2+\frac{h}{Bk}\right)^{\frac{1}{2}}z\right)-\frac{\sinh\left(\left(\left(\frac{n\pi}{W}\right)^2+\frac{h}{Bk}\right)^{\frac{1}{2}}L\right)}{\cosh\left(\left(\left(\frac{n\pi}{W}\right)^2+\frac{h}{Bk}\right)^{\frac{1}{2}}L\right)}\sinh\left(\left(\left(\frac{n\pi}{W}\right)^2+\frac{h}{Bk}\right)^{\frac{1}{2}}z\right)\right]. \quad (3\text{-}45)$$

Equation 3-45 can be factored into Equation 3-46 and a new constant, C_n, is defined.

$$Z_n(z)=\frac{A_n}{\cosh\left(\left(\left(\frac{n\pi}{W}\right)^2+\frac{h}{Bk}\right)^{\frac{1}{2}}L\right)}\left[\cosh\left(\left(\left(\frac{n\pi}{W}\right)^2+\frac{h}{Bk}\right)^{\frac{1}{2}}z\right)\cosh\left(\left(\left(\frac{n\pi}{W}\right)^2+\frac{h}{Bk}\right)^{\frac{1}{2}}L\right)-\sinh\left(\left(\left(\frac{n\pi}{W}\right)^2+\frac{h}{Bk}\right)^{\frac{1}{2}}L\right)\sinh\left(\left(\left(\frac{n\pi}{W}\right)^2+\frac{h}{Bk}\right)^{\frac{1}{2}}z\right)\right] \quad (3\text{-}46)$$

$$C_n=\frac{A_n}{\cosh\left(\left(\left(\frac{n\pi}{W}\right)^2+\frac{h}{Bk}\right)^{\frac{1}{2}}L\right)} \quad \text{for n=0, 1, 2, …, } \infty. \quad (3\text{-}47)$$

Based on the hyperbolic function identity $\cosh(x)\cosh(y)-\sinh(x)\sinh(y)=\cosh(x-y)$

Equation 3-46 simplifies to, for n= 1, 2, 3…

$$Z_n(z)=\frac{C_0}{2}\cosh\left(\left(\frac{h}{Bk}\right)^{\frac{1}{2}}(L-z)\right)+C_n\cosh\left(\left(\left(\frac{n\pi}{W}\right)^2+\frac{h}{Bk}\right)^{\frac{1}{2}}(L-z)\right) \quad (3\text{-}48)$$

Combining Y_n and Z_n and summing for n from 0 to infinity leads to Equation 3-49.

$$\theta_s(y,z)=\frac{C_0}{2}\cosh\left(\left(\frac{h}{Bk}\right)^{\frac{1}{2}}(L-z)\right)+\sum_{n=1}^{\infty}C_n\cos\left(\frac{n\pi y}{W}\right)\cosh\left(\left(\left(\frac{n\pi}{W}\right)^2+\frac{h}{Bk}\right)^{\frac{1}{2}}(L-z)\right) \quad (3\text{-}49)$$

The last boundary condition is the function that describes T_{wall}. The exponential functionality from Equation 3-11 will be used to describe T_{wall} as a function of y, as shown in Equation 3-50.

$$\theta_s(y,0)=e^{-\beta y} \quad (3\text{-}50)$$

Substituting this function into Equation 3-49 for z=0 lead to

$$\theta_s(y,0)=\frac{C_0}{2}\cosh\left(\left(\frac{h}{Bk}\right)^{\frac{1}{2}}L\right)+\sum_{n=0}^{\infty}C_n\cos\left(\frac{n\pi y}{W}\right)\cosh\left(\left(\left(\frac{n\pi}{W}\right)^2+\frac{h}{Bk}\right)^{\frac{1}{2}}L\right)=e^{-\beta y} \tag{3-51}$$

Using a Fourier transformation, Equation 3-51 becomes for n=1, 2, 3, …

$$C_n\cosh\left(\left(\left(\frac{n\pi}{W}\right)^2+\frac{h}{Bk}\right)^{\frac{1}{2}}L\right)=\frac{2}{W}\int_0^W e^{-\beta y}\cos\left(\frac{n\pi y}{W}\right)dy \tag{3-52}$$

Integration and application of limits leads to Equation 3-54.

$$C_n\cosh\left(\left(\left(\frac{n\pi}{W}\right)^2+\frac{h}{Bk}\right)^{\frac{1}{2}}L\right)=\frac{2}{W}\left[\frac{e^{-\beta y}\left(-\beta\cos\left(\frac{n\pi y}{W}\right)+\left(\frac{n\pi}{W}\right)\sin\left(\frac{n\pi y}{W}\right)\right)}{\beta^2+\left(\frac{n\pi}{W}\right)^2}\right]_{y=0}^{y=W} \tag{3-53}$$

$$C_n\cosh\left(\left(\left(\frac{n\pi}{W}\right)^2+\frac{h}{Bk}\right)^{\frac{1}{2}}L\right)=\frac{2}{W}\left[\frac{e^{-\beta y}\left(-\beta\cos(n\pi)+\left(\frac{n\pi}{W}\right)\sin(n\pi)\right)-(-\beta)}{\beta^2+\left(\frac{n\pi}{W}\right)^2}\right] \tag{3-54}$$

Solving for C_n yields Equation 3-55.

$$C_n=\frac{2\beta\left((-1)^{n+1}e^{-\beta W}+1\right)}{W\left(\beta^2+\left(\frac{n\pi}{W}\right)^2\right)\cosh\left(\left(\left(\frac{n\pi}{W}\right)^2+\frac{h}{Bk}\right)^{\frac{1}{2}}L\right)} \tag{3-55}$$

The final two-dimensional fit equation becomes Equation 3-56.

$$\theta_s(y,z)=\frac{C_0}{2}\cosh\left(\left(\frac{h}{Bk}\right)^{\frac{1}{2}}(L-z)\right)+\sum_{n=1}^{\infty}C_n\cos\left(\frac{n\pi y}{W}\right)\cosh\left(\left(\left(\frac{n\pi}{W}\right)^2+\frac{h}{Bk}\right)^{\frac{1}{2}}(L-z)\right) \tag{3-56}$$

Equation 3-56 can then be used to develop a model from experimental surface temperature data. The parameters to be determined are β and the group of variables (h/Bk). The rest of the variables in the model can be found by physical measurement. The parameters were evaluated by minimizing the squared error between model surface temperature and actual surface temperature from infrared camera data. The parameter β describes the wall temperature profile, which is influenced by the fluid flow. The group of variables (h/Bk) combines the surface convection from the fin with the conduction through the fin to create a variable group that describes the fin behavior.

A comparison of the model temperature profiles based on the analytical analysis to the experimental infrared thermal images is shown in Figure 3-8. The figure shows two-dimensional temperature plots for half of the panel. The plots show that the analytical profile is able to successfully model the data, fitting well in both dimensions, supporting the validity of Equation 3-56.

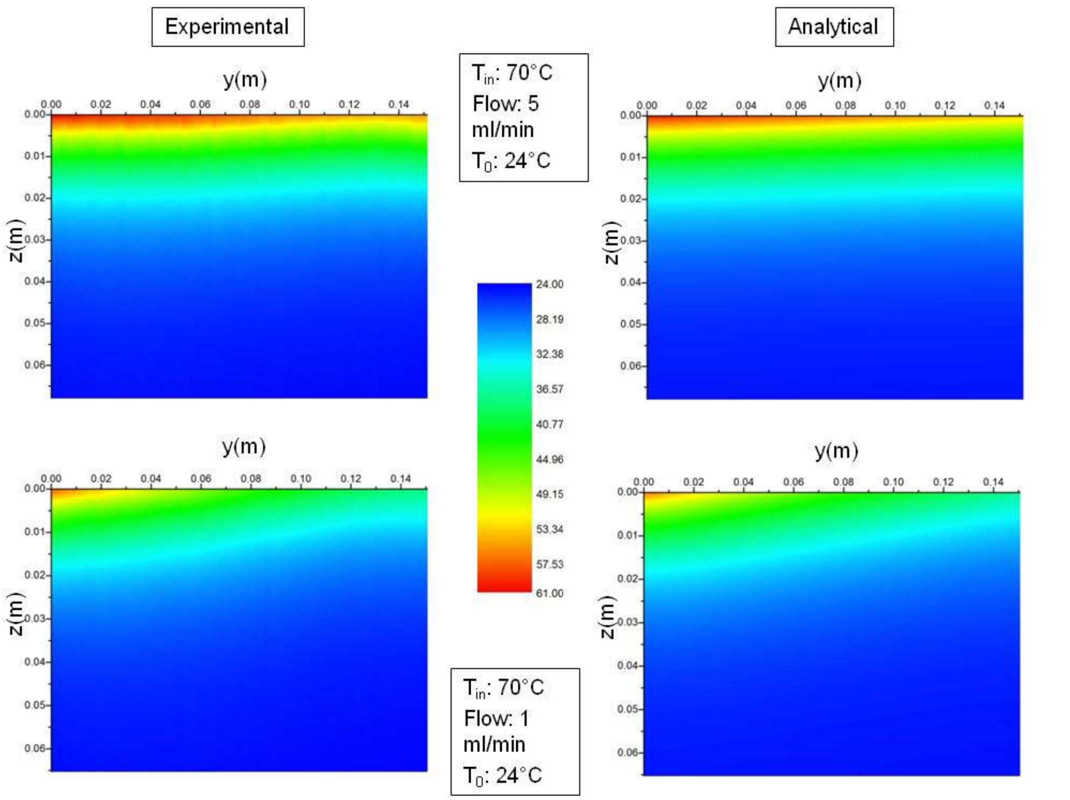

Figure 3-8: 2D temperature profile comparison of experimental thermal images to analytical fit

3.3.3. Pressure Drop Analysis of Temperature Profile

Using the isothermal pressure drop data that was collected and the Hagen-Poiseuille equation, Equation 3-57, the inside diameter of each tube can be determined for each lined panel. The pressure drop is denoted by ($-\Delta P$). Volumetric flow rate (V_y) and fluid viscosity (μ) are used.

$$D_1 = \frac{128\mu W V_y}{\pi(-\Delta P)} \tag{3-57}$$

A diameter was found for each panel by minimizing the error between the experimental pressure drop and the theoretical pressure drop based on the Hagen-Poiseuille equation. The results are shown in Table 3-1. This analysis was unable to be performed on the unlined panel due to the pressure drop inconsistencies created by the restrictive inlet and outlet fixtures.

Table 3-1: Summary of diameters from pressure drop calculations

Panel (listed dimensions)	Actual ID
0.004" ID, 0.008" OD	0.0045" (113 μm)
0.005" ID, 0.010" OD	0.0061" (154 μm)
0.010" ID, 0.016" OD	0.0099" (252 μm)

In order to further validate the exponential fit of the tube temperature profile, the non-isothermal pressure drop data can be compared to the expected results from the Hagen-Poiseuille equation. By using a correlating for the dependence of the viscosity of water on temperature and numerically integrating over the length of the panel, the pressure drop for the non-isothermal panels can be determined. Comparing these predictions to the experimental pressure drop values provides insight on the accuracy of the exponential temperature profile fit. Tables 3-2, 3-3, and 3-4 show these results

Table 3-2: Experimental pressure drop and outlet temperature comparison to fit for 0.004” ID, 0.008” OD panel

0.004" ID, 0.008" OD							
T_0=30 °C							
Flow rate (mL/min)	Experimental ΔP (MPa)	Fit ΔP (MPa)	Percent Difference	Experimental Outlet Temp. (°C)	Fit Outlet Temp. (°C)	Percent Difference (%)	Average Re
4	3.1647	3.0672	-3.18	29.6	29.3	-1.12	928.7
3	2.3091	2.3132	0.18	29.0	28.8	-0.80	692.6
2	1.5072	1.5539	3.00	28.0	28.1	0.39	458.3
1	0.7474	0.7931	5.77	26.1	26.5	1.34	224.6
0.5	0.3821	0.4052	5.69	24.6	25.0	1.69	110.0
0.25	0.1999	0.2069	3.38	24.1	24.0	-0.43	53.9
0.125	0.1033	0.1051	1.77	23.7	23.5	-0.87	26.5
T_0=50 °C							
5	3.1282	2.7127	-15.32	46.1	45.8	-0.65	1652.9
4	2.4187	2.1923	-10.32	44.9	44.7	-0.47	1309.2
3	1.7340	1.6677	-3.98	43.5	43.2	-0.70	968.5
2	1.1307	1.1438	1.14	40.1	40.4	0.66	628.6
1	0.5964	0.6125	2.63	33.1	34.4	3.73	295.3
0.5	0.3285	0.3350	1.96	26.9	28.3	4.93	136.5
0.25	0.1742	0.1814	3.97	24.8	24.8	0.11	63.7
T_0=70 °C							
5	2.9937	2.0614	-45.23	62.6	61.3	-2.09	2196.0
4	1.9064	1.6701	-14.15	60.5	59.9	-0.99	1735.5
3	1.3810	1.2928	-6.83	56.9	55.9	-1.78	1263.5
2	0.8846	0.8932	0.96	52.2	52.2	-0.04	815.5
1	0.4908	0.5019	2.23	39.6	41.7	5.10	369.5

Table 3-3: Experimental pressure drop and outlet temperature comparison to fit for 0.005” ID, 0.010” OD panel

0.005" ID, 0.010" OD							
T_0=30 °C							
Flow rate (mL/min)	Experimental ΔP (MPa)	Fit ΔP (MPa)	Percent Difference	Experimental Outlet Temp. (°C)	Fit Outlet Temp. (°C)	Percent Difference (%)	Average Re
8	1.5741	1.4768	-6.59	29.7	29.7	0.00	1372.6
4	0.7274	0.7424	2.03	29.0	29.1	0.46	682.5
2	0.3475	0.3758	7.54	27.7	27.9	0.78	337.1
1	0.1874	0.1913	2.02	25.8	26.4	2.26	165.6
0.5	0.0978	0.0978	0.06	24.5	24.8	1.16	81.0
0.25	0.0520	0.0500	-3.89	24.0	23.6	-1.60	39.6
T_0=50 °C							
8	1.1942	1.0353	-15.35	47.5	47.0	-1.06	1972.3
4	0.5350	0.5278	-1.38	44.6	44.6	0.02	967.4
2	0.2776	0.2749	-0.98	39.6	40.0	0.99	465.2
1	0.1484	0.1475	-0.61	32.8	33.4	1.81	218.2
0.5	0.0834	0.0806	-3.49	26.9	27.3	1.56	100.9
T_0=70 °C							
10	2.1519	0.9709	-121.63	65.7	64.7	-1.51	3318.1
8	1.3886	0.7852	-76.84	64.4	63.0	-2.24	2625.9
4	0.4399	0.4068	-8.14	58.5	57.9	-1.08	1268.6
2	0.2215	0.2156	-2.72	50.3	50.5	0.41	601.3
1	0.1219	0.1191	-2.38	38.7	40.4	4.28	276.2

Table 3-4: Experimental pressure drop and outlet temperature comparison to fit for 0.010” ID, 0.016” OD panel

0.01" ID, 0.016" OD							
T_0=30 °C							
Flow rate (mL/min)	**Experimental ΔP (MPa)**	**Fit ΔP (MPa)**	**Percent Difference**	**Experimental Outlet Temp. (°C)**	**Fit Outlet Temp. (°C)**	**Percent Difference (%)**	**Average Re**
12	0.3774	0.3695	-2.14	29.6	29.9	1.03	1263.0
8	0.2386	0.2471	3.44	29.3	29.7	1.18	839.6
4	0.1156	0.1242	6.98	28.8	29.1	1.11	417.4
2	0.0587	0.0629	6.61	27.8	28.0	0.64	206.1
1	0.0314	0.0321	1.93	26.2	26.5	1.14	101.1
0.5	0.0175	0.0164	-6.77	24.8	24.9	0.54	49.5
0.25	0.0106	0.0084	-26.87	24.3	23.8	-1.96	24.2
T_0=50 °C							
12	0.2843	0.2582	-10.13	48.5	47.6	-1.90	1821.0
8	0.1786	0.1739	-2.72	47	46.6	-0.81	1201.9
4	0.0851	0.0890	4.37	44.3	44.2	-0.30	587.4
2	0.0445	0.0467	4.69	39.3	39.3	0.08	280.3
1	0.0234	0.0251	6.46	32.8	33.7	2.59	131.6
0.5	0.0148	0.0137	-7.39	26.7	27.6	3.40	60.8
T_0=70 °C							
12	0.2830	0.1933	-46.39	67.2	65.9	-1.96	2456.0
8	0.1407	0.1312	-7.22	65.5	63.1	-3.84	1608.3
4	0.0674	0.0681	1.02	59.1	58.8	-0.47	775.1
2	0.0357	0.0365	2.06	51.3	51.0	-0.62	364.0
1	0.0196	0.0206	4.82	38.4	40.6	5.35	164.5

3.3.4. Separating Internal and Surface Resistance from Total Resistance

In order to separate the individual heat transfer coefficients associated with each step in the heat transfer from the fluid to the atmosphere from the overall heat transfer coefficient, U, it is necessary to solve for the total resistance through that portion of the system. Solving for the individual resistances is desirable so that the major resistance to heat transfer can be identified in order to make improvements that will enhance heat transfer.

First, the tube-side heat load can be determined by using Equation 3-58.

$$Q_{tube} = 2\pi r_1 U \int_0^W \left(T_f(y) - T_o\right) dy \tag{3-58}$$

Substitution of Equation 3-59, a form of Equation 3-11, into Equation 3-58 and integration leads to Equation 3-60, where r_1 is the inside radius of the tube.

$$T_f(y) - T_0 = \left(T_{1f} - T_0\right) e^{-\beta y} \tag{3-59}$$

$$Q_{tube} = \frac{2\pi r_1 U}{\beta}\left(T_{1f} - T_0\right)\left(1 - e^{-\beta W}\right) \tag{3-60}$$

The internal heat load based on the heat transfer from bulk fluid to inner wall of the tube can be determined based on Equation 3-61. The internal heat transfer coefficient is represented by U_i. This combines the factors affecting heat transfer from the fluid to the surface.

$$Q_i = 2\pi r_1 \int_0^W U_i \left(T_f(y) - T_s(y)\right) dy \tag{3-61}$$

By combing the temperature profiles from Equations 3-62 and 3-63, T_f-T_s can be found.

$$T_s(y) = T_0 + (T_{1s} - T_0)e^{-\beta y} \tag{3-62}$$

$$T_f(y) = T_0 + (T_{1f} - T_0)e^{-\beta y} \tag{3-63}$$

$$T_f(y) - T_s(y) = (T_{1f} - T_{1s})e^{-\beta y} \tag{3-64}$$

Inserting Equation 3-64 into Equation 3-61 yields

$$Q_i = 2\pi r_1 U_i \int_0^W (T_{1f} - T_{1s})e^{-\beta y}\,dy \tag{3-65}$$

Integration leads to

$$Q_i = \frac{2\pi r_1 U_i (T_{1f} - T_{1s})}{\beta}\left(1 - e^{-\beta W}\right) \tag{3-66}$$

Another heat load can be determined based on $T_s(y)$ at z=0. Using the heat transfer area shown in Figure 3-9 and overall surface heat transfer coefficient U_s, which combines the conduction in the z-direction with convective heat transfer at the panel surface, half of the panel heat load can be determined by Equation 3-67.

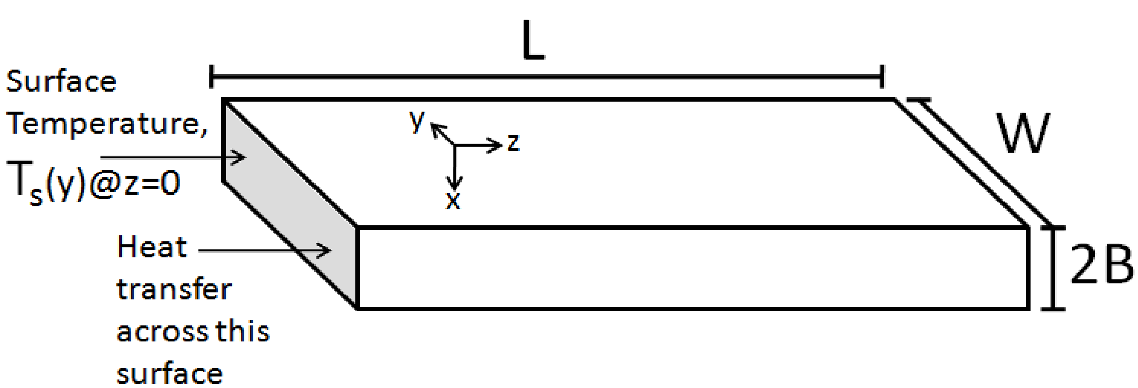

Figure 3-9: Illustration of geometry on which overall surface heat transfer coefficient (U_s) is based.

$$Q_{s,\frac{1}{2}} = \int_0^W 2BU_s\left(T_s(y) - T_0\right)dy \tag{3-67}$$

Substituting a form of Equation 3-50 into Equation 3-67 leads to

$$Q_{s,\frac{1}{2}} = 2BU_s \int_0^W (T_{1s} - T_0) e^{-\beta y} dy \tag{3-68}$$

Integration gives Equation 3-69.

$$Q_{s,\frac{1}{2}} = \frac{2BU_s (T_{1s} - T_0)}{\beta} \left(1 - e^{-\beta W}\right) \tag{3-69}$$

Accounting for both halves of the panel

$$Q_s = 2Q_{s,\frac{1}{2}} = \frac{4BU_s (T_{1s} - T_0)}{\beta} \left(1 - e^{-\beta W}\right) \tag{3-70}$$

Since heat load is fixed in the system, the three heat transfer coefficients, U, U_i, and U_s, can be related by Equation 3-72.

$$Q_s = Q_i = Q_{tube} = Q \tag{3-71}$$

$$\frac{(T_{1f} - T_0)(1 - e^{-\beta W})}{Q} = \frac{(T_{1f} - T_{1s})(1 - e^{-\beta W})}{Q} + \frac{(T_{1s} - T_0)(1 - e^{-\beta W})}{Q} \tag{3-72}$$

Substituting for Q from Equations 3-60, 3-66, and 3-70, respectively, leads to

$$\frac{\beta}{2\pi r_1 U} = \frac{\beta}{2\pi r_1 U_i} + \frac{\beta}{4BU_s} \tag{3-73}$$

Simplification leads to Equation 3-74, written in series resistance form. Equations 3-75 to 3-77 show the overall, internal, and surface resistances, respectively.

$$\frac{1}{U} = \frac{1}{U_i} + \frac{\pi r_1}{2BU_s} \tag{3-74}$$

$$R_{total} = \frac{1}{U} \qquad R_i = \frac{1}{U_i} \qquad R_s = \frac{\pi r_1}{2BU_s} \qquad \text{(3-75 – 3-77)}$$

Using heat load, calculated from the experimental temperature difference data, as shown in Equation 3-78, all three heat transfer coefficients can be determined, where $\dot{m}$ is the mass flow rate of water.

$$Q = \dot{m}Cp\left(T_{1f} - T_{2f}\right) \tag{3-78}$$

Equations 3-60, 3-70, and 3-74, respectively, are rewritten in the following forms

$$U = \frac{\beta Q}{2\pi r_1\left(T_{1f} - T_0\right)}\left(1 - e^{-\beta W}\right)^{-1} \tag{3-79}$$

$$U_s = \frac{\beta Q}{4B\left(T_{1s} - T_0\right)}\left(1 - e^{-\beta W}\right)^{-1} \tag{3-80}$$

$$U_i = \frac{1}{2\pi r_1}\left(\frac{1}{2\pi r_1 u} - \frac{1}{4Bu_s}\right)^{-1} \tag{3-81}$$

The heat transfer coefficients based on the experimental heat load are shown graphically in Figure 3-10.

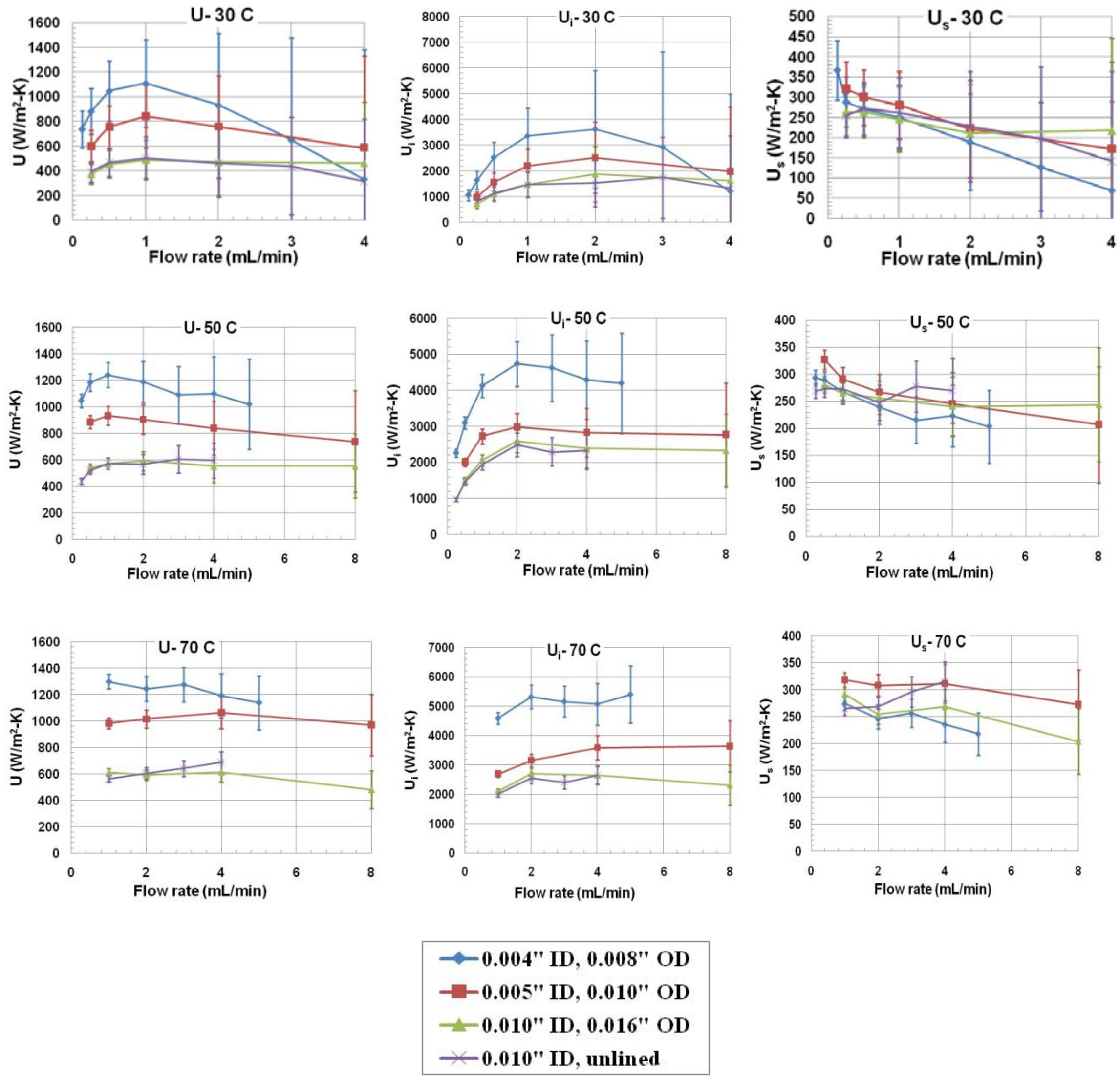

Figure 3-10: Total, internal, and surface heat transfer coefficients (*U*, U_i, U_s) for all tube sizes and inlet temperatures.

Table 3-5 shows a comparison between the internal and surface resistances, as a percentage of the overall resistance. Figure 3-11 shows a graphical comparison of the two resistances.

Table 3-5: Comparing Internal (R_i) to Surface (R_s) Resistance as a Percentage of Total Resistance for All Tube Sizes and Inlet Temperatures

0.004" ID, 0.008" OD			
T_{1f}	Flowrate (mL/min)	R_i (%)	R_s (%)
30	4	27.69	72.31
30	3	22.31	77.69
30	2	25.65	74.35
30	1	32.97	67.03
30	0.5	41.45	58.55
30	0.25	53.83	46.17
30	0.125	69.64	30.36
50	5	24.27	75.73
50	4	25.61	74.39
50	3	23.58	76.42
50	2	25.06	74.94
50	1	30.03	69.97
50	0.5	38.15	61.85
50	0.25	46.16	53.84
70	5	21.09	78.91
70	4	23.49	76.51
70	3	24.73	75.27
70	2	23.42	76.58
70	1	28.34	71.66

0.005" ID, 0.010" OD			
T_{1f}	Flowrate (mL/min)	R_i (%)	R_s (%)
30	8	30.64	69.36
30	4	29.65	70.35
30	2	29.96	70.04
30	1	38.32	61.68
30	0.5	48.27	51.73
30	0.25	61.55	38.45
50	8	26.65	73.35
50	4	29.68	70.32
50	2	30.33	69.67
50	1	34.21	65.79
50	0.5	44.27	55.73
70	10	25.99	74.01
70	8	26.64	73.36
70	4	29.65	70.35
70	2	32.20	67.80
70	1	36.51	63.49

0.010" ID, 0.016" OD			
T_{1f}	Flowrate (mL/min)	R_i (%)	R_s (%)
30	12	26.93	73.07
30	8	27.51	72.49
30	4	28.36	71.64
30	2	25.08	74.92
30	1	33.14	66.86
30	0.5	41.87	58.13
30	0.25	52.32	47.68
50	12	21.65	78.35
50	8	23.75	76.25
50	4	23.10	76.90
50	2	22.82	77.18
50	1	27.73	72.27
50	0.5	35.83	64.17
70	12	19.16	80.84
70	8	20.82	79.18
70	4	23.15	76.85
70	2	21.88	78.12
70	1	29.33	70.67

0.010" ID, unlined			
T_{1f}	Flowrate (mL/min)	R_i (%)	R_s (%)
30	4	24.13	75.87
30	3	25.13	74.87
30	2	30.61	69.39
30	1	34.64	65.36
30	0.5	41.34	58.66
30	0.25	47.79	52.21
50	4	25.40	74.60
50	3	26.36	73.64
50	2	22.71	77.29
50	1	29.28	70.72
50	0.5	35.50	64.50
50	0.25	44.99	55.01
70	4	25.99	74.01
70	3	26.60	73.40
70	2	23.60	76.40
70	1	28.04	71.96

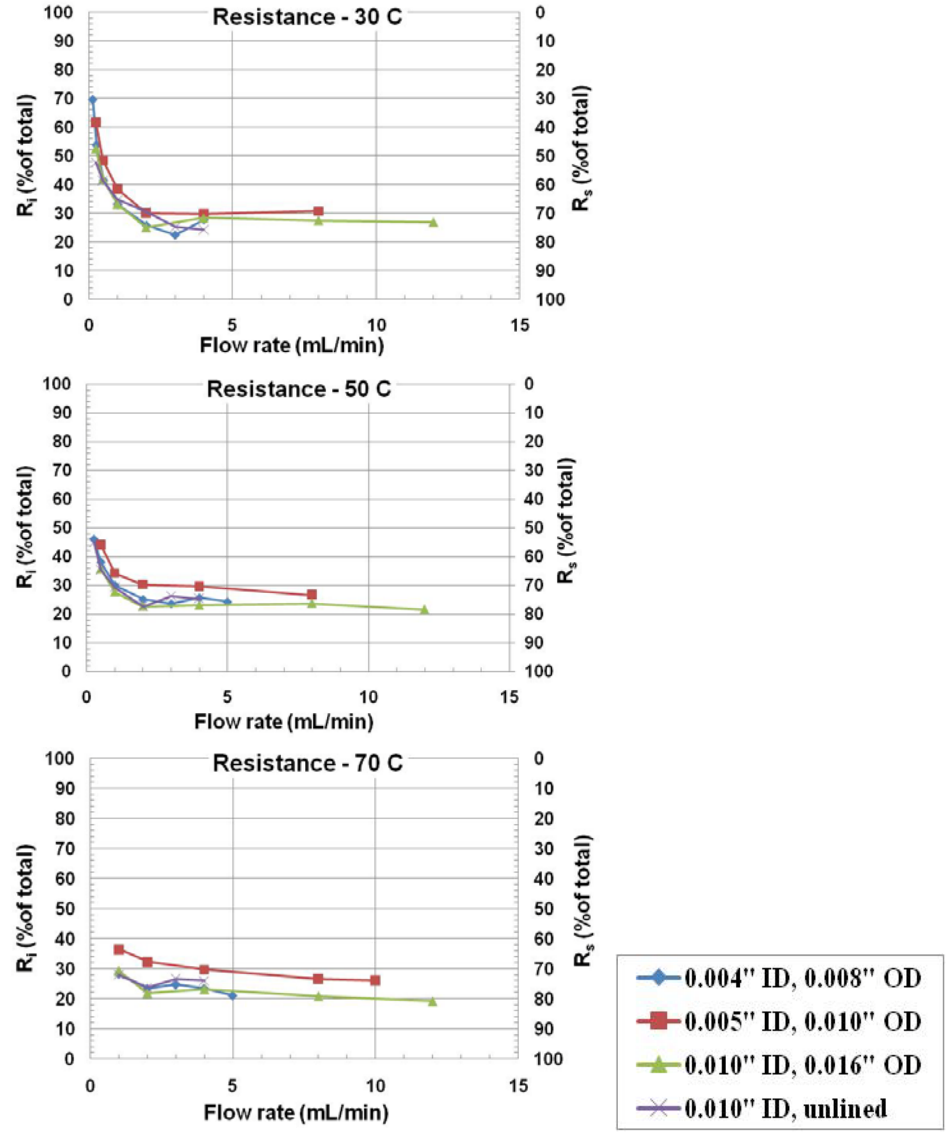

Figure 3-11: Comparing Internal (R_i) to Surface (R_s) Resistance as a Percentage of Total Resistance for All Tube Sizes and Inlet Temperatures

The graph shows that the effect of internal resistance diminishes as flow rate increases. Under most flow conditions, surface heat transfer accounts for 70-80 % of the total resistance. It is only at very low flow rates that internal resistance plays a more substantial role in the overall resistance.

3.3.5. Further Analysis of Internal Resistance

It is possible to further explore the internal heat transfer coefficient by separating the total internal resistance (R_i) into the three resistances shown in Figure 3-11, is given by Equation 3-82.

$$R_i = \left(R_1 + R_{1,2} + R_2\right) \tag{3-82}$$

R_1 is the resistance to heat transfer at the fluid-solid interface inside the tube. $R_{1,2}$ is the resistance due to conduction through the tube wall. R_2 is the combined resistance due to the tube-composite interface as well as the conduction from the outer tube wall to the surface in the "transition region" from cylindrical to rectangular coordinates. Based on the radius of the inside of the tube, the total internal resistance becomes Equation 3-83, where h_1 is the individual tube side heat transfer coefficient, k_t is the thermal conductivity of the tube, and u_2 is an individual heat transfer coefficient that combines conduction, interfacial resistance, and the geometry transition.

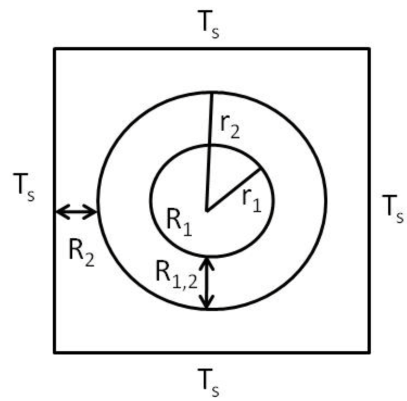

Figure 3-12: Internal heat transfer resistances in series

$$R_i = \frac{1}{U_i} = \left(\frac{1}{h_1} + \frac{r_1 \ln\left(r_2 / r_1\right)}{k_t} + \frac{r_1}{r_2 u_2}\right) \tag{3-83}$$

By assuming that u_2 is approximately constant for all tube and flow conditions, u_2 can be solved for by equating h_1, in the form of Equation 3-84, for the stainless steel lined 0.01" ID panel with the 0.01" ID unlined panel for each matching flow conditions.

$$h_1 = r_1^{-1}\left(\frac{1}{r_1 U_i} - \frac{\ln(r_2/r_1)}{k_t} - \frac{1}{r_2 u_2}\right)^{-1} \tag{3-84}$$

The average h_2 from these calculations was then used to solve for h_1 under all tube and flow conditions. Table 3-6 shows the results of these calculations. Also tabulated is the resistance due to fluid-solid heat transfer from the water to the tube or unlined passage as a percentage of the total resistance. As can be seen in the table, this resistance accounts for nearly all of the internal resistance to heat transfer.

Table 3-6: Table of tube side heat transfer coefficient (h_1) and tube side resistance (R_1) as a percentage of total internal resistance (R_i)

0.004" ID, 0.008" OD			
T_{1f}	Flow rate (mL/min)	h_1 (W/m^2-K)	R_1 (%)
30	4	1209	99.73
30	3	2951	99.35
30	2	3655	99.20
30	1	3389	99.26
30	0.5	2541	99.44
30	0.25	1644	99.64
30	0.125	1061	99.77
50	5	4241	99.08
50	4	4331	99.06
50	3	4670	98.98
50	2	4788	98.96
50	1	4167	99.09
50	0.5	3123	99.32
50	0.25	2277	99.50
70	5	5469	98.81
70	4	5134	98.88
70	3	5221	98.86
70	2	5383	98.83
70	1	4635	98.99

0.005" ID, 0.010" OD			
T_{1f}	Flow rate (mL/min)	h_1 (W/m^2-K)	R_1 (%)
30	8	1081	99.73
30	4	1996	99.50
30	2	2538	99.36
30	1	2210	99.44
30	0.5	1571	99.60
30	0.25	978	99.75
50	8	2791	99.30
50	4	2849	99.28
50	2	3008	99.24
50	1	2746	99.31
50	0.5	2016	99.49
70	10	3540	99.11
70	8	3679	99.08
70	4	3629	99.09
70	2	3184	99.20
70	1	2713	99.32

0.010" ID, 0.016" OD			
T_{1f}	Flow rate (mL/min)	h_1 (W/m^2-K)	R_1 (%)
30	12	1645	99.37
30	8	1903	99.28
30	4	1653	99.37
30	2	1898	99.28
30	1	1488	99.43
30	0.5	1096	99.58
30	0.25	719	99.73
50	12	1894	99.28
50	8	2357	99.10
50	4	2414	99.08
50	2	2616	99.01
50	1	2078	99.21
50	0.5	1511	99.42
70	12	2288	99.13
70	8	2336	99.11
70	4	2687	98.98
70	2	2737	98.96
70	1	2115	99.20

0.010" ID, unlined			
T_{1f}	Flow rate (mL/min)	h_1 (W/m^2-K)	R_1 (%)
30	4	1315	99.99
30	3	1743	99.98
30	2	1526	99.98
30	1	1462	99.98
30	0.5	1139	99.99
30	0.25	824	99.99
50	4	2345	99.97
50	3	2296	99.98
50	2	2498	99.97
50	1	1955	99.98
50	0.5	1470	99.98
50	0.25	975	99.99
70	4	2657	99.97
70	3	2414	99.97
70	2	2564	99.97
70	1	2012	99.98

3.3.6. Further Analysis of Surface Resistance

In order to further examine the overall surface heat transfer coefficient, an expression can be developed for U_s in terms of h and k. The heat load from the panel due to natural convection can be determined using Equation 3-85.

$$Q_{panel} = 4h\int_0^W\int_0^L (T_s - T_0)\,dz\,dy \tag{3-85}$$

Substituting a form of the expression for θ_s from Equation 3-50 into Equation 3-85 leads to

$$Q_{panel} = 4h(T_{1s} - T_0)\int_0^W\int_0^L\left(\frac{C_0}{2}\cosh\left(\left(\frac{h}{Bk}\right)^{\frac{1}{2}}(L-z)\right) + \sum_{n=1}^{\infty} C_n \cos\left(\frac{n\pi y}{W}\right)\cosh\left(\left(\left(\frac{n\pi}{W}\right)^2 + \frac{h}{Bk}\right)^{\frac{1}{2}}(L-z)\right)\right)dzdy \tag{3-86}$$

Double integration of Equation 3-87 and simplification leads to Equation 3-90.

$$Q_{panel} = 4h(T_{1s} - T_0)\int_0^W\left[-\frac{C_0}{2\left(\frac{h}{Bk}\right)^{\frac{1}{2}}}\sinh\left(\left(\frac{h}{Bk}\right)^{\frac{1}{2}}(L-z)\right) + \sum_{n=1}^{\infty} - \frac{C_n}{\left(\frac{n^2\pi^2}{W^2} + \frac{h}{Bk}\right)^{\frac{1}{2}}}\cos\left(\frac{n\pi y}{W}\right)\sinh\left(\left(\left(\frac{n\pi}{W}\right)^2 + \frac{h}{Bk}\right)^{\frac{1}{2}}(L-z)\right)\right]_{z=0}^{z=L} dy \tag{3-87}$$

$$Q_{panel} = 4h(T_{1s} - T_0)\left[\frac{C_0}{2\left(\frac{h}{Bk}\right)^{\frac{1}{2}}}\sinh\left(\left(\frac{h}{Bk}\right)^{\frac{1}{2}}L\right)y + \sum_{n=1}^{\infty}\frac{C_n}{\left(\frac{n^2\pi^2}{W^2} + \frac{h}{Bk}\right)^{\frac{1}{2}}\left(\frac{n\pi}{W}\right)}\sin\left(\frac{n\pi y}{W}\right)\sinh\left(\left(\left(\frac{n\pi}{W}\right)^2 + \frac{h}{Bk}\right)^{\frac{1}{2}}L\right)\right]_{y=0}^{y=W} \tag{3-88}$$

$$Q_{panel} = 4h(T_{1s} - T_0)\left[\frac{C_0}{2\left(\frac{h}{Bk}\right)^{\frac{1}{2}}}\sinh\left(\left(\frac{h}{Bk}\right)^{\frac{1}{2}}L\right)W + \sum_{n=1}^{\infty}\frac{C_n}{\left(\frac{n^2\pi^2}{W^2} + \frac{h}{Bk}\right)^{\frac{1}{2}}\left(\frac{n\pi}{W}\right)}\sin(n\pi)\sinh\left(\left(\left(\frac{n\pi}{W}\right)^2 + \frac{h}{Bk}\right)^{\frac{1}{2}}L\right)\right] \tag{3-89}$$

$$Q_{panel} = 2C_0W(T_{1s} - T_0)(hBk)^{\frac{1}{2}}\sinh\left(\left(\frac{h}{Bk}\right)^{\frac{1}{2}}L\right) \tag{3-90}$$

Substituting C_0 from Equation 3-55 yields

$$Q_{panel} = \frac{4(T_{1s} - T_0)(hBk)^{\frac{1}{2}}}{\beta_s}\tanh\left(\left(\frac{h}{Bk}\right)^{\frac{1}{2}}L\right)\left(1 - e^{-\beta_s W}\right) \tag{3-91}$$

Equating Q_s, from Equation 3-70, with Q_{panel} leads to

$$\frac{4Bu_s(T_{1s} - T_0)}{\beta}\left(1 - e^{-\beta W}\right) = \frac{4(T_{1s} - T_0)(hBk)^{\frac{1}{2}}}{\beta_s}\tanh\left(\left(\frac{h}{Bk}\right)^{\frac{1}{2}}L\right)\left(1 - e^{-\beta_s W}\right) \tag{3-92}$$

Rearranging leads to an expression for the overall surface heat transfer coefficient in terms of the surface heat transfer coefficient, *h*, and the panel thermal conductivity, *k*.

$$U_s = \left(\frac{hk}{B}\right)^{\frac{1}{2}} \tanh\left(\left(\frac{h}{Bk}\right)^{\frac{1}{2}} L\right) \tag{3-93}$$

Dividing by *k* and rearranging gives an expression for *k* in terms of U_s and *h/Bk* in Equation 3-94.

$$\frac{U_s}{k} = \left(\frac{h}{Bk}\right)^{\frac{1}{2}} \tanh\left(\left(\frac{h}{Bk}\right)^{\frac{1}{2}} L\right) \tag{3-94}$$

$$k = U_s \left[\left(\frac{h}{Bk}\right)^{\frac{1}{2}} \tanh\left(\left(\frac{h}{Bk}\right)^{\frac{1}{2}} L\right)\right]^{-1} \tag{3-95}$$

The overall surface heat transfer coefficient, U_s, has been previously determined via Equation 3-80. *h/Bk* is a variable grouping that was a parameter in the 2-dimensional surface temperature model. Therefore, *k* can be calculated based on Equation 3-95. The surface heat transfer coefficient can then also be determined from *k* and *h/Bk*. Table 3-7 shows a comparison of the surface heat transfer coefficient, *h*, from the previous method and *h* calculated by numerically integrating the experimental temperature profile from the infrared camera.

Table 3-7: Table comparing surface heat transfer coefficients determined by different methods

0.004" ID, 0.008" OD			
T_{1f}	Flow rate (mL/min)	h, from heat load	h, from surface temperature
30	4	2.50	2.42
30	3	4.51	4.57
30	2	6.74	6.81
30	1	9.57	9.60
30	0.5	9.70	9.28
30	0.25	10.80	9.60
30	0.125	15.43	12.72
50	5	7.24	7.22
50	4	7.84	7.87
50	3	7.71	7.73
50	2	8.46	8.44
50	1	9.33	9.22
50	0.5	10.20	9.99
50	0.25	9.99	9.36
70	5	8.01	7.99
70	4	8.52	8.50
70	3	9.11	9.09
70	2	8.74	8.67
70	1	9.58	9.45

0.005" ID, 0.010" OD			
T_{1f}	Flow rate (mL/min)	h_s, from heat load	h_s, from surface temperature
30	8	3.62	3.82
30	4	6.17	6.43
30	2	7.73	8.00
30	1	10.26	10.33
30	0.5	11.08	10.68
30	0.25	13.02	10.83
50	8	7.54	7.68
50	4	8.69	8.91
50	2	9.55	9.73
50	1	10.52	10.43
50	0.5	11.87	11.64
70	10	9.37	9.73
70	8	9.99	10.27
70	4	11.72	12.07
70	2	11.25	11.59
70	1	11.10	11.28

0.010" ID, 0.016" OD			
T_{1f}	Flowrate (mL/min)	h_s, from heat load	h_s, from surface temperature
30	12	6.96	7.17
30	8	8.08	8.29
30	4	7.47	7.62
30	2	6.93	7.03
30	1	8.62	8.52
30	0.5	8.88	8.50
30	0.25	8.48	7.25
50	12	6.28	6.56
50	8	8.69	9.04
50	4	8.30	8.48
50	2	9.20	9.39
50	1	8.98	9.04
50	0.5	9.34	9.19
70	12	6.46	6.62
70	8	7.32	7.48
70	4	9.49	9.69
70	2	8.97	9.20
70	1	10.12	10.27

0.010" ID, unlined			
T_{1f}	Flow rate (mL/min)	h_s, from heat load	h_s, from surface temperature
30	4	4.88	4.89
30	3	6.73	6.70
30	2	8.00	8.00
30	1	8.93	8.73
30	0.5	9.47	9.02
30	0.25	7.20	6.48
50	4	8.84	8.80
50	3	9.25	9.12
50	2	8.30	8.24
50	1	8.85	8.66
50	0.5	8.47	8.28
50	0.25	7.53	7.14
70	4	11.08	10.91
70	3	10.04	9.79
70	2	8.96	8.88
70	1	8.66	8.54

Table 3-7 indicates good agreement between the experimental values for the individual surface heat transfer coefficient and the values based on the 2-dimensional fit parameter *h/Bk* and the calculated value of *U*

Chapter IV: Conclusion and Future Work

4.1. Mechanical

The results from the Mode I mechanical analysis shows that no toughness is sacrificed by embedding the tubes in the panel. Therefore, there is no penalty to introducing the added heat transfer functionality of the microvascular tubes. Further exploration is necessary to determine if inter-laminar sheer strength is compromised by creating the unlined channels.

4.2. Thermal – Multiple Tube Panels

The main goal of the multiple tube panel was achieved. Using typical aerospace materials under standard processing techniques, a panel was created with 24 embedded tubes (102 μm ID/203 μm OD). Cooling fluid entered and exited the system via a single inlet and outlet and displayed significant cooling potential under practical conditions (as high as 3 kW/m^2). Creating a panel with multiple unlined channels by the same means would be the next step in demonstrating capability.

4.3. Thermal – Single Tube Panels

A two-dimensional model of the single tube panels was developed and validated by experimental data. The exponential functionality of the tube temperature profile was supported by comparing experimental pressure drop data with pressured drop values based on model temperature profiles. The two-dimensional temperature profile matches experimental infrared images.

The capability to create a single unlined passage was developed. This passage was created under standard processing conditions. It was also demonstrated that the heat transfer properties of the unlined passage are not appreciably different than stainless steel tubes of the same size. Therefore, this shows that the stainless tube does not offer significant thermal resistant and that the tube and composite are in good thermal contact.

Total and individual heat transfer coefficient calculations were able to identify the main heat transfer resistances in the hybrid system. About three-fourths of the total heat transfer resistance is due to surface heat transfer. This is equally influenced by the surface heat transfer coefficient and the composite thermal conductivity. Increasing each would lead to lower resistance.

The other quarter of the resistance is due to the internal resistance of the panel, which is almost completely due to the cooling fluid to surface heat transfer coefficient. Increasing this will reduce the heat transfer resistance.

WORKS CITED

[1] Kousarakis, A., Mouritz, A.P. and Bannister, M.K. (2006). Interlaminar properties of polymer laminates containing internal sensor cavities, *Composite Structures* **75**(1-4): 610-618.

[2] Kousarakis, A., Mouritz, A.P. and Bannister, M.K. (2008). Tensile and compressive properties of laminates containing internal sensor cavities, *Composites: Part A* **39**(9): 1394-1403.

[3] Pang, J.W.C. and Bond, I.P. (2005). 'Bleeding composites' – damage detection and self repair using biomimetic approach, *Composites: Part A* **36**(2): 183-188.

[4] Pang, J.W.C. and Bond, I.P. (2005). A hollow fiber reinforced polymer composite encompassing self-healing and enhanced damage visibility, *Composites Science and Technology* **65**(11-12): 1791-1799.

[5] Dry, C. (1996). Procedures developed for self-repair of polymer matrix composite materials, *Composite Structure* **35**(3): 263-269.

[6] Motuku, M., Validya, U.K. and Janowski, G.M. (1999). Parametric studies on self-repairing approaches for resin infused composites subjected to low velocity impact, *Smart Materials and Structures* **8**(5): 623-638.

[7] Bleay, S.M., Loader, C.B., Hawyes, V.J., Humberstone, L. and Curtis, P.T. (2001). A smart repair system for polymer matrix composites, *Composites: Part A* **32**(12): 1767-1776.

[8] Trask, R.S. and Bond, I.P. (2006). Biomimetic self-healing of advanced composite structures using hollow glass fibres, *Smart Materials and Structures* **15**(3):704-710.

[9] Williams, G., Trask, R. and Bond, I. (2007). A self-healing carbon fibre reinforced polymer for aerospace applications, *Composites: Part A* **38**(6): 1525-1532.

[10] Williams, H.R., Trask, R.S. and Bond, I.P. (2007). Self-healing composite sandwich structures, *Smart Materials and Structures* **16**(4): 1198-1207.

[11] Williams, H.R., Trask, R.S. and Bond, I.P. (2008). Self-healing sandwich panels: Restoration of compressive strength after impact, *Composite Science and Technology* **68**(15-16): 3171-3177.

[12] Toohey, K.S., Sottos, N.R., Lewis, J.A., Moore, J.S. and White, S.R. (2007). Self-healing materials with microvascular networks, *Nature Materials* **6**(8): 581-585.

[13] Toohey, K.S., Hansen, C.J., Lewis, J.A., White, S.R. and Sottos, N.R. (2009). Delivery of two-part self-healing chemistry via microvascular networks, *Advanced Functional Materials* **19**(9): 1399-1405.

[14] Hansen, C.J., Wu, W., Toohey, K.S., White, S.R., Sottos, N.R. and Lewis, J.A. (2009). Self healing materials with interpenetrating microvascular networks, *Advanced Materials* **21**: 4143-4147.

[15] Tuckerman, D.B. and Pease, F.W. (1981). High-performance heat sinking for VLSI, *IEEE Electron Device Letters* **2**(5): 126-129.

[16] Ashman, S. and Kandlikar, S.G. (2006) A review of manufacturing processes for microchannel heat exchanger fabrication, In: *Proceedings of Fourth International Conference on Nanochannels, Microchannels and Minichannels*, 855-860, June 19-21, 2006.

[17] Paul, B.K., Kwon, P., and Subramanian, R. (2006). Understanding limits on fin aspect ratios in counterflow microchannel arrays produced by diffusion bonding, *Journal of Manufacturing Science and Engineering, Transactions of the ASME* **128**(4): 977-983.

[18] Qi, H., Chen, T., Yao, L. and Zuo, T. (2009). Micromachining of microchannel on the polycarbonate substrate with CO_2 direct write laser ablation, *Optics and Lasers in Engineering*, **47**(5): 594-598.

[19] Lee, P., Garimella, S.V. and Liu, D. (2005). Investigation of heat transfer in rectangular microchannels, *International Journal of Heat and Mass Transfer* **48**(9): 1688-1704.

[20] Lelea, D., Nishio, S. and Takano, K. (2004). The experimental research on microtube heat transfer and fluid flow of distilled water, *International Journal of Heat and Mass Transfer* **47**(12-13): 2817-2830

[21] Wei, X.J., Joshi, Y. and Patterson, M.K. (2007) Experimental and numerical study of a stacked microchannel heat sink for liquid cooling of microelectric devices, *Journal of Heat Transfer-Transactions of the ASME* **129**(10): 1432-1444.

[22] Oueslati, R.B., Therriault, D. and Martel, S. (2008) PCB-integrated heat exchanger for cooling electronics using microchannels fabricated with the direct-write method, *IEEE Transactions on Components and Packaging Technologies* **31**(4): 869-874.

[23] Kozola, B.D., Natrajan, V.K., Christensen, K.T. and White, S.R. (2008). Active cooling of polymer structures using microvascular networks, *Society of Engineering Science Annual Technical Meeting*, October 12-15.